

RC-LACE stay report

Optimizing the performance of sub-kilometer ALARO Canonical Model Configuration

Mario Hrastinski

In collaboration with: Petra Smoliková and Radmila Brožková

2-13 December 2024.

CHMI, Prague, Czech Republic

1 Introduction

During this stay, the pseudo-3D turbulence code in the TOUCANS scheme [1, 2] of the ALARO Canonical Model Configuration (CMC) [3] was further revised and tested. Sensitivity experiments were carried out at various horizontal grid spacings: $\Delta x = 4, 2, 1,$ and 0.5 km. Additionally, the impact and adaptation of the 3MT scheme were explored across resolutions, particularly focussing on $\Delta x = 1$ and 0.5 km. This report is structured as follows: Section 2 describes the components of the pseudo-3D turbulence scheme and the formulation of the horizontal turbulence length scale. Section 3 details the numerical model setup, while Section 4 presents the analysis of results. Finally, Section 5 provides concluding remarks.

2 The pseudo-3D turbulence in the ALARO CMC

The pseudo-3D turbulence scheme in the ALARO CMC incorporates two main components: (i) the inclusion of horizontal shear effects in the production of a pair of turbulence energies [4, 5] (see Subsection 2.1), and (ii) the additional, i.e., horizontal, 2D diffusion equation [6] (see Subsection 2.2). Additionally, a unified Horizontal Turbulence Length Scale (HTLS) formulation is applied consistently to both components, following [7] (see Subsection 2.3).

2.1 *Introducing the horizontal effects to the production of turbulence energies*

The initial implementation of the horizontal shear effects to a pair of prognostic turbulence energies within the TOUCANS scheme is described in [8]. Here, we provide only details relevant

to the current work. The 3D shear production term (I_{3D}) in prognostic equations for Turbulence Kinetic Energy (TKE) and turbulence total energy can be expressed as follows:

$$I_{3D} = - \underbrace{\frac{u'w'}{\partial z} \frac{\partial \bar{u}}{\partial z} - \frac{v'w'}{\partial z} \frac{\partial \bar{v}}{\partial z}}_{I_{\text{vert}}} - \underbrace{\frac{u'u'}{\partial x} \frac{\partial \bar{u}}{\partial x} - \frac{u'v'}{\partial y} \frac{\partial \bar{u}}{\partial y} - \frac{u'v'}{\partial x} \frac{\partial \bar{v}}{\partial x} - \frac{v'v'}{\partial y} \frac{\partial \bar{v}}{\partial y}}_{I_{\text{horiz}}} \quad (1)$$

where the prime stands for turbulent perturbations from the mean state (overbar), while the averaged products of turbulent perturbations are called turbulence fluxes (of momentum in this case). Following the work of [9], [4, 5] parametrized the horizontal component of shear production term (I_{horiz}) as:

$$I_{\text{horiz}} = (L_H^K)^2 \cdot \left[\left(\frac{\partial u}{\partial x} \right)^2 + \left(\frac{\partial v}{\partial y} \right)^2 + \frac{1}{2} \left(\frac{\partial u}{\partial y} + \frac{\partial v}{\partial x} \right)^2 \right]^{\frac{3}{2}} \quad (2)$$

where L_H^K is HTLS, while u and v are horizontal wind components.

2.2 The 1D+2D turbulence scheme

The 1D+2D turbulence scheme within TOUCANS is derived assuming $\frac{\partial K_{M/H,hor}}{\partial x} + \frac{\partial K_{M/H,hor}}{\partial y} = 0$ and is available in the IAL code for a long time. It combines the vertical and horizontal (red terms) effects of turbulence as follows:

$$\frac{\partial u_i}{\partial t} + \dots = -K_{M,hor} \frac{\partial^2 u_i}{\partial x^2} - K_{M,hor} \frac{\partial^2 u_i}{\partial y^2} + \frac{\partial}{\partial z} (\overline{w'u'_i}) \quad (3)$$

$$\frac{\partial \Psi}{\partial t} + \dots = -K_{H,hor} \frac{\partial^2 \Psi}{\partial x^2} - K_{H,hor} \frac{\partial^2 \Psi}{\partial y^2} + \frac{\partial}{\partial z} (\overline{w'\Psi'}) \quad (4)$$

$$\overline{w'u'_i} = -K_{M,ver} \frac{\partial u_i}{\partial z} \quad (5)$$

$$\overline{w'\Psi'} = -K_{H,ver} \frac{\partial \Psi}{\partial z} + \text{TOMs} \quad (6)$$

$$K_{M,ver} = L_K C_K \sqrt{e_k} \chi_3(\text{Ri}), \quad K_{H,ver} = L_K C_K C_3 \sqrt{e_k} \phi_3(\text{Ri}) \quad (7)$$

$$K_{M,hor} = L_K^H C_K^H \sqrt{e_k} \chi_{3,hor}(\text{Ri}), \quad K_{H,hor} = L_K^H C_K^H C_3 \sqrt{e_k} \phi_{3,hor}(\text{Ri}) \quad (8)$$

where u_i and Ψ denote horizontal wind components ($u_1=u$ and $u_2=v$) and scalar variables (temperature and humidity); χ_3 , $\chi_{3,\text{hor}}$, ϕ_3 and $\phi_{3,\text{hor}}$ are vertical and horizontal stability dependency functions (see 1, 6); L_K is vertical turbulence length scale; e_k is TKE; C_3 is inverse Prandtl number at neutrality; C_K and C_K^H are closure constants affecting the magnitude of turbulence fluxes and terms in prognostic equations for turbulence energies. It is assumed $C_K^H = C'_K \cdot C_K$ and we start with $C'_K=1$, i.e., $C_K^H = C_K$. The computation of horizontal operators in Eqs. (3)-(4) is performed on η levels by SLHD. Additionally, the computation for wind components is also possible on z levels.

2.3 The horizontal turbulence length scale

The HTLS formulation used in the above two approaches is based on the work of [7] and made dependent on properties of the local flow (shear and stretching):

$$L_{H_{\text{shr}}} = sW \left[\left(\frac{\partial v}{\partial x} \right)^2 + \left(\frac{\partial u}{\partial y} \right)^2 \right]^{-\frac{1}{2}}, \quad L_{H_{\text{str}}} = sW \left[\left(\frac{\partial u}{\partial x} \right)^2 + \left(\frac{\partial v}{\partial y} \right)^2 \right]^{-\frac{1}{2}} \quad (9)$$

where $L_{H_{\text{shr}}}$ and $L_{H_{\text{str}}}$ are shear and stretching HTLSs, while s is a Resolution-Dependent Correction Factor (RDCF), compensating for the application of finite differences method in the computation horizontal derivatives (in their model). The RDCF is computed as follows:

$$s = \left(\frac{\Delta_0}{\Delta} \right)^\alpha \quad (10)$$

where Δ_0 is the grid spacing at which the model can resolve the most energetic turbulent eddies ($\Delta_0=100$ m), Δ is a grid spacing of the actual model, and α is an empirical constant chosen so that the resulting HTLS is comparable to that derived from observations. In our case, the latter remains as given by [7], i.e., $\alpha=1.45$. The combined HTLS is derived by averaging the $L_{H_{\text{shr}}}$ and $L_{H_{\text{str}}}$:

$$L_H^{K'} = \sqrt{L_{H_{\text{shr}}} L_{H_{\text{str}}}} \quad (11)$$

and protected against too big values that may pose a problem for numerical stability:

$$L_H^K = \max \left(L_H^{K'}, c_s \sqrt{\Delta} \right) \quad (12)$$

where $c_s=0.20-0.25$ is Smagorinsky's constant. Following previous tests and the need for a stronger pseudo-3D scheme, we opt for $c_s=1.0$, evaluating the impact later.

3 Numerical model setup

In this study, we employ the ALARO CMC with a non-hydrostatic dynamical core and the ALARO-1vB physics package across four domains with $\Delta x = 4, 2, 1,$ and 0.5 km, respectively. All domains cover approximately the same area (Fig. 1a). To investigate resolved and subgrid TKE with consistent data sampling, simulations use a uniform time step of $\Delta t = 15$ s. For other experiments, such as evaluating the impact of the 3MT scheme, $\Delta x = 150, 75, 40,$ and 20 s, respectively.

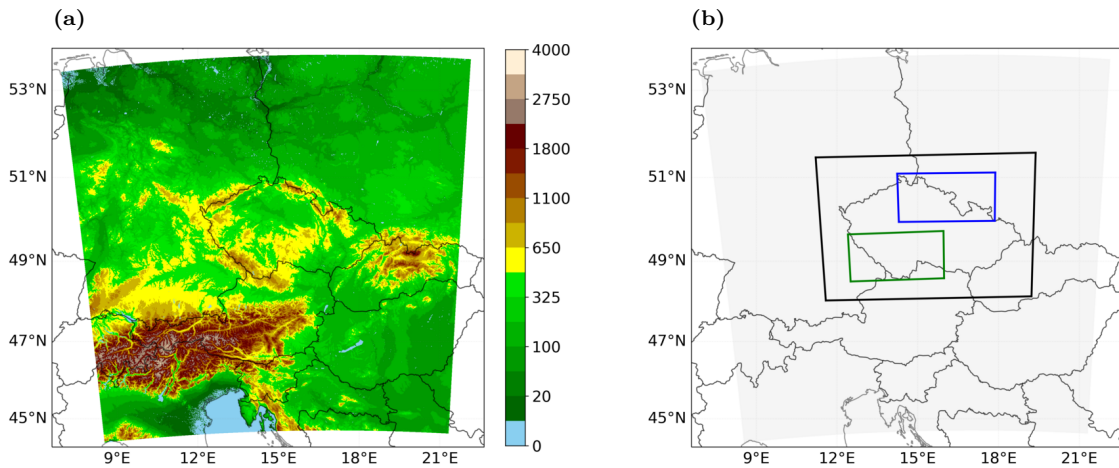


Figure 1: (a) Orography of the model domain at $\Delta x = 1$ km and (b) sub-domains for computation of resolved TKE (TKE_{res} ; blue and green rectangle) and convective condensation fluxes (black rectangle).

The model was initialized on 21 June 2018 and 10 June 2023 at 00 UTC and integrated over a 24-hour period, using the 87 vertical levels of a hybrid mass-based and terrain-following coordinate η . Initial conditions are obtained by interpolating the operational ALARO-CZ model fields from $\Delta x = 2.325$ km to the target resolution. Lateral boundary conditions are provided by the global model ARPEGE, with a 3-hour coupling frequency. The simulations focus on two convective systems passing through regions denoted by blue (21 June 2018) and green (10 June 2023) rectangles in Fig. 1b. The first case is initiated along the frontal system moving from west to east, while the second is a more localized event that developed without the synoptic-scale forcing.

4 The results of numerical simulations

For the analysis of the two simulations, the following diagnostic tools were employed: (i) chosen 3D prognostic fields (pressure departure, horizontal wind components and precipitation), (ii) Kinetic Energy Spectra (KES) computed using ECTO, and (iii) vertical profiles of resolved (TKE_{res}), subgrid (TKE_{subg}), and total TKE (TKE_{tot}). The profiles of the latter were averaged over a sub-domain indicated by the two small rectangles in Fig. 1b. Finally, to study the impact of the 3MT scheme, convective condensation fluxes were averaged over the area marked by the larger black rectangle.

4.1 The impact of tuning the pseudo-3D turbulence scheme

As shown during the previous stay, i.e., [10], the impact of the pseudo-3D scheme in TOUCANS is small when using its default settings. Therefore, we abandon the initial assumption that $C_K^H = C_K$, i.e., $C_K' = 1$. Further, we explore the impact of (i) limitation of L_K^H in Eq. (12), (ii) computation of horizontal wind derivatives and (iii) orographic roughness length.

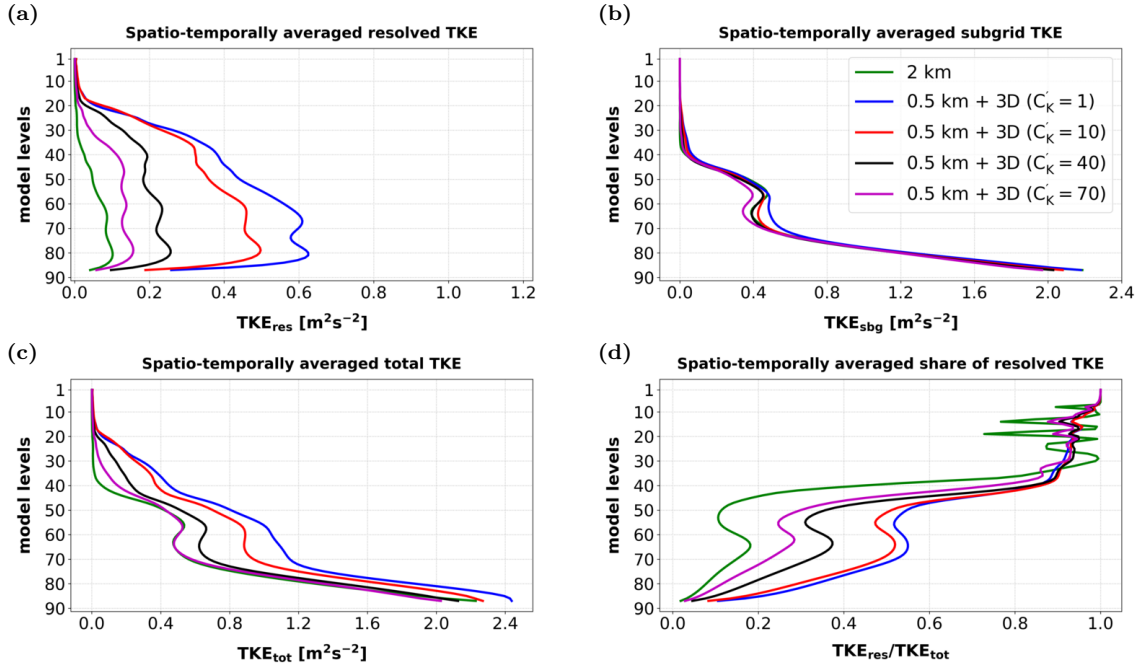


Figure 2: Spatially (over blue rectangle in Fig. 1b) and temporally (between 14:00 and 16:00 UTC) averaged: (a) resolved TKE, (b) subgrid TKE, (c) total TKE and (d) share of resolved TKE at $\Delta x = 2$ km and various experiments at $\Delta x = 0.5$ km (see legend) for the forecast initialized at 00 UTC 21 June 2018.

With the increase of C'_K parameter, the impact of the 1D + 2D scheme increases, thereby considerably reducing TKE_{res} (Fig. 2a). At the same time, TKE_{sbg} is also slightly reduced (Fig. 2b), whereas TKE_{tot} nearly matches the reference at $\Delta x = 2$ km (Fig. 2c). In addition, the KES analysis points to a removal of energy near the tail of the spectrum for levels in the lower and middle troposphere (Fig. 3a-b). Consistently, the pressure departure fields suggest that the amount of small-scale features is reduced (not shown). This is further supported by the 6-hour accumulated precipitation, with the associated fields showing enhanced agreement with observations (Fig. 4a-c).

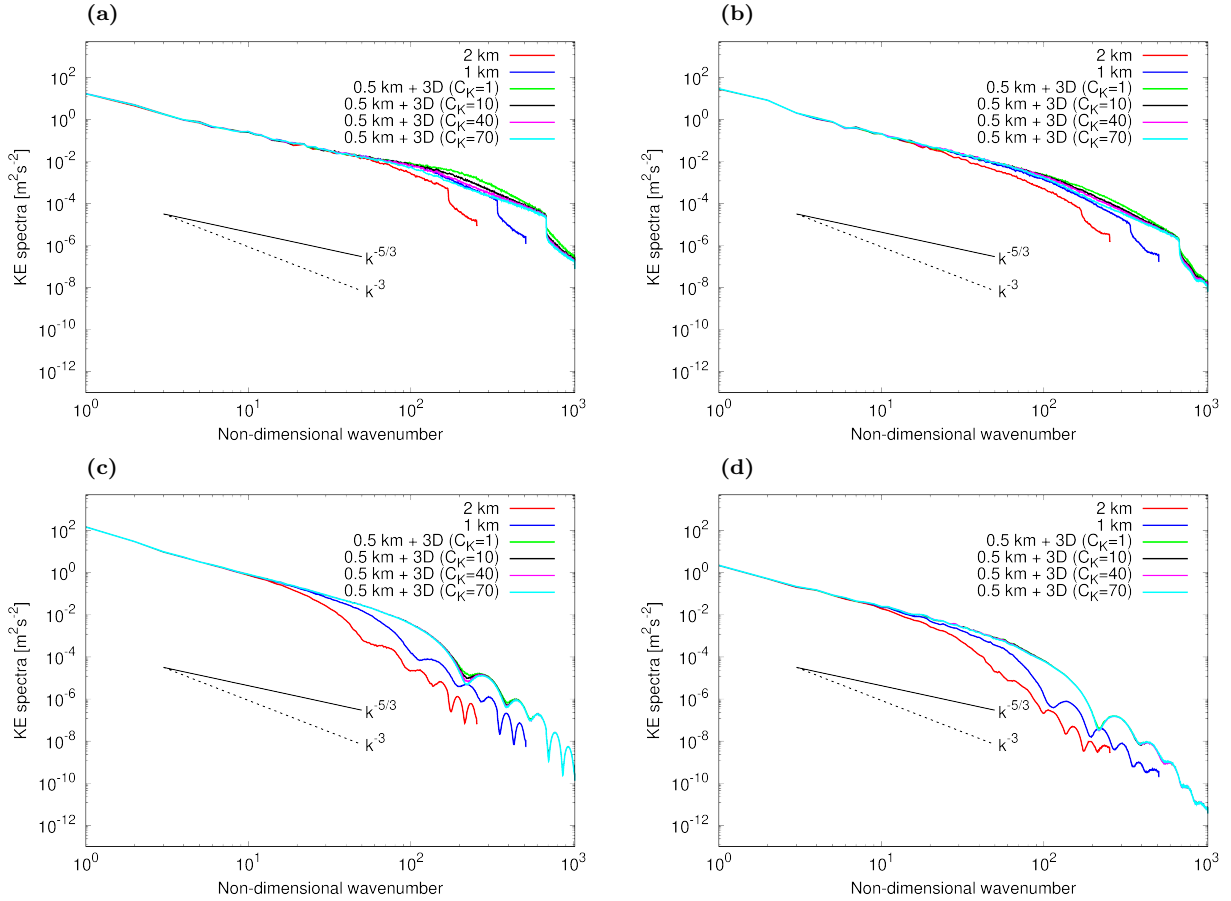


Figure 3: Kinetic energy spectra at 15 UTC on 21 June 2018 for the reference at $\Delta x = 2$ km and various sensitivity tests at $\Delta x = 0.5$ km, corresponding to different intensities of the pseudo-3D turbulence scheme, given by the parameter C'_K . Results are shown at the following model levels: (a) 80, (b) 50, (c) 20 and (d) 10.

The influence of protecting $L_H^{K'}$ in Eq. (12) on TKE_{res} and TKE_{tot} is substantial (Fig. 5a-d). The impact on KES and analyzed fields is similar but somewhat smaller than that of

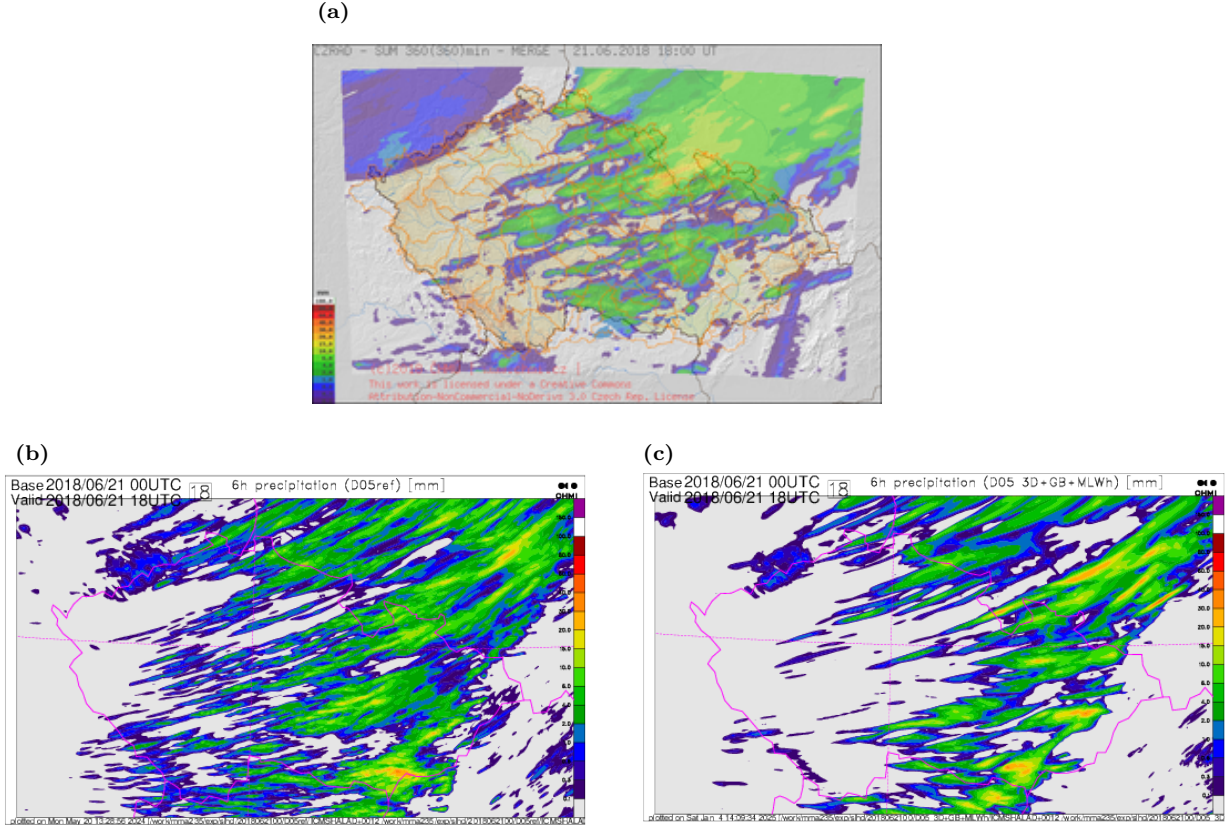


Figure 4: 6-hour accumulated total precipitation, i.e., between 12 UTC and 18 UTC on 21 June 2018 for: (a) observations and $\Delta x=0.5$ [km] experiments with (b) $C'_K=1$ and (c) $C'_K=70$.

the C'_K tuning (not shown). Additionally, we examined the impact of the method to compute horizontal wind derivatives. In the original approach, calculations were performed at constant η levels, while Petra's modifications allow for computations at constant height (iso- z) levels. The influence on TKE_{res} and TKE_{tot} is rather small (Fig. 6a-d), although using the "iso- z " approach results in a better match with the 2km reference near the surface. A comparable impact can be achieved by increasing the orographic roughness length (Fig. 7a-d). However, this results in an increase of TKE_{res} and TKE_{tot} in the middle and upper troposphere.

For the 10 June 2023 case, only the combined impact of $C'_K=70$ and $c_s=1$ was tested. The analysis indicates that the pseudo-3D scheme is overly intense, with TKE_{res} approaching the 2 km reference too closely, while TKE_{tot} is lower than the reference (not shown). Additional investigation of the pseudo-3D scheme settings is necessary.

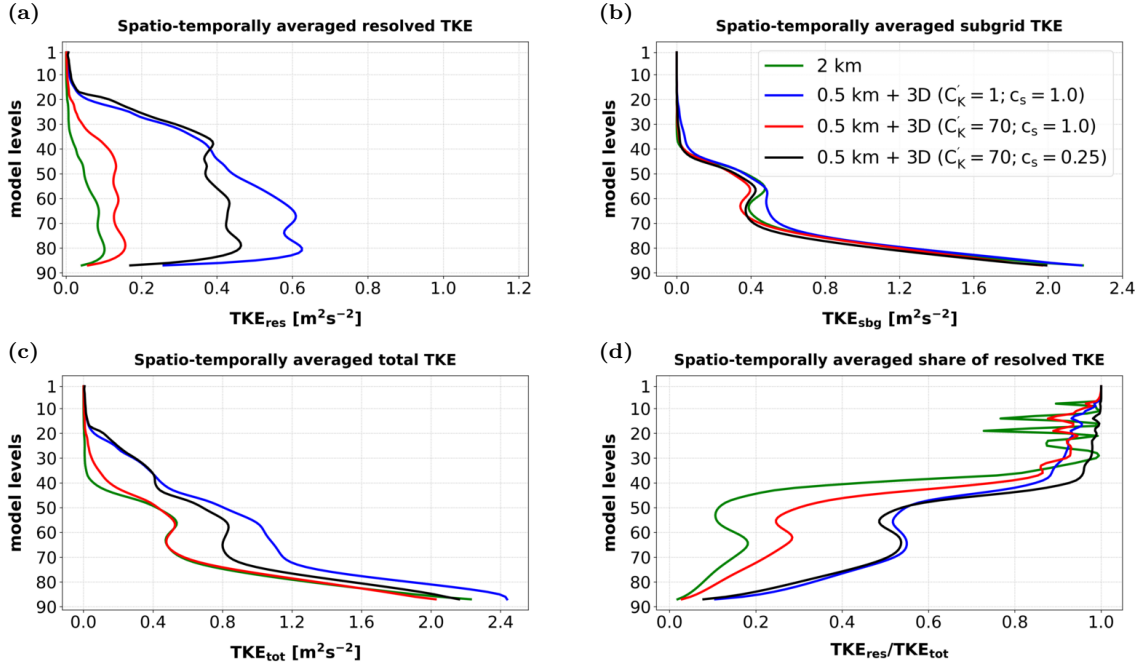


Figure 5: Spatially (over blue rectangle in Fig. 1b) and temporally (between 14:00 and 16:00 UTC) averaged: (a) resolved TKE, (b) subgrid TKE, (c) total TKE and (d) share of resolved TKE at $\Delta x=2$ km and various experiments at $\Delta x=0.5$ km (see legend) for the forecast initialized at 00 UTC 21 June 2018.

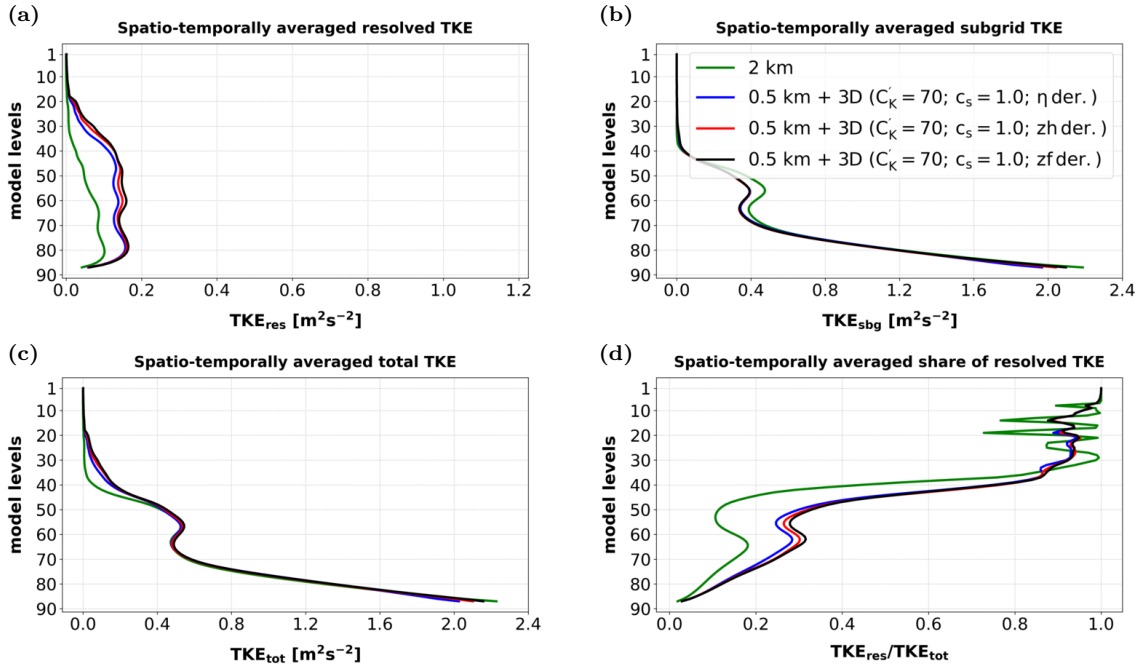


Figure 6: Spatially (over blue sub-domain on Fig. 1b) and temporally (between 14:00 and 16:00 UTC) averaged: (a) resolved TKE, (b) subgrid TKE, (c) total TKE and (d) share of resolved TKE at $\Delta x=2$ km and various experiments at $\Delta x=0.5$ km (see legend) for the forecast initialized at 00 UTC 21 June 2018. There are two implementations of iso-z level derivatives, i.e., at half (hl) and full (fl) model levels.

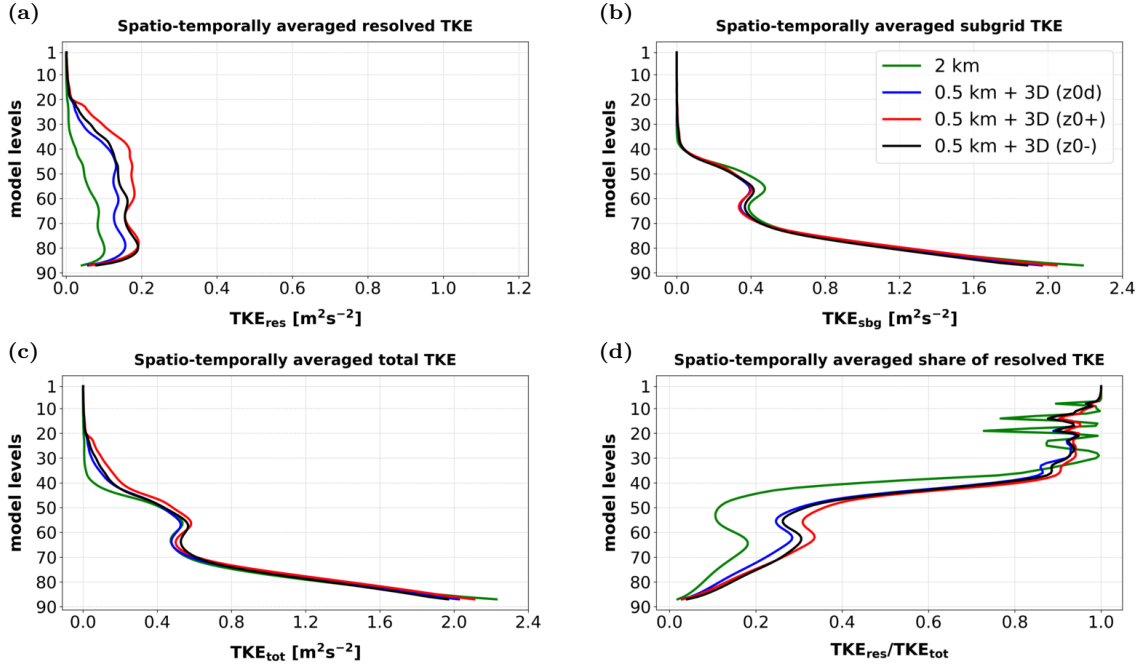


Figure 7: Spatially (over blue sub-domain on Fig. 1b) and temporally (between 14:00 and 16:00 UTC) averaged: (a) resolved TKE, (b) subgrid TKE, (c) total TKE and (d) share of resolved TKE at $\Delta x=2$ km and various experiments at $\Delta x=0.5$ km (see legend) for the forecast initialized at 00 UTC 21 June 2018.

4.2 Investigating the impact of the 3MT scheme

Given that previous experiments, e.g., [11], highlighted the role of the 3MT scheme at $\Delta x = 0.5$ km and 1 km, we proceed with a more detailed evaluation of its impact. First, we test the scheme’s behavior across resolutions, followed by switching it off at (sub)-kilometric Δx , i.e., where the deep convection is expected to be mostly resolved by the model’s dynamic core.

4.2.1 The adaptation of convective condensation flux across resolutions

Analysis of resolved (grid-scale) and unresolved (subgrid-scale) convective condensation fluxes at $\Delta x = 4, 2, 1,$ and 0.5 km for the 21 June 2018 case suggests that the 3MT scheme adapts only slightly to a decrease in Δx (Fig. 8a-d). Furthermore, the total condensation flux grows with the increasing grid-scale contribution. Note also that at higher resolutions, the peak of the grid-scale component appears earlier, while its buildup is sharper.

To adjust the 3MT scheme’s adaptation to higher resolution, we (i) modified the closure parameter RMULACVG ($5.5 \rightarrow 4.0$), (ii) switched off the contribution of the downdraught

component (LCDDPRO=.F.), and (iii) enabled only triggering by the dynamical contribution (LCVGQD=.T.). However, only the impact of (i) was notable, although still insufficient, resulting in a decrease in the subgrid-scale and an increase in the grid-scale component of convective condensation flux (not shown). In contrast, the impact on the precipitation patterns was minor. Finally, in the 10 June 2023 case, the adaptation of the 3MT scheme across resolution is substantially weaker, resulting in a dominant subgrid-scale contribution even at $\Delta x=0.5$ km (not shown). Further investigation and tuning are foreseen.

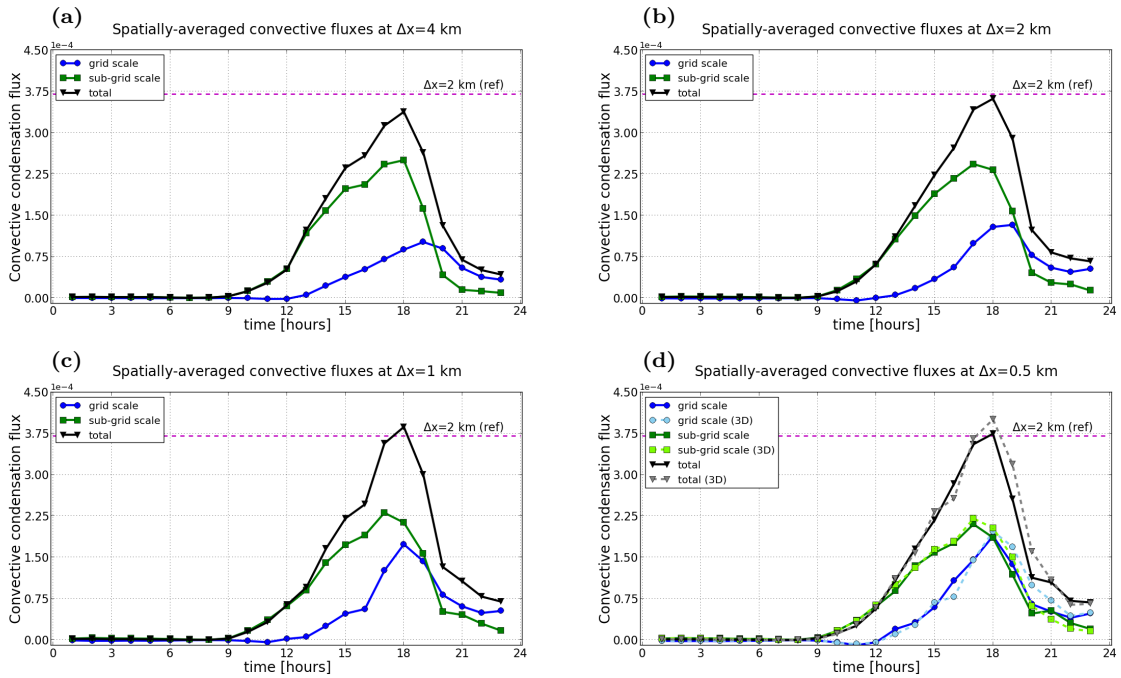


Figure 8: Spatially averaged subgrid-scale, grid-scale and total convective condensation flux during the 21 June 2018 convection case at: (a) $\Delta x=4$ km, (b) $\Delta x=2$ km, (c) $\Delta x=1$ km and (d) $\Delta x=0.5$ km.

4.2.2 The impact of switching off the 3MT scheme

Finally, we approach a more comprehensive study of the 3MT scheme’s impact as a whole, starting with the case of 21 June 2018. Note that in all further tests, the pseudo-3D scheme is not active. When the 3MT scheme is switched off, the subdomain-averaged total convective condensation remains nearly the same, i.e., the grid-scale component takes over (Fig. 9a-b). In addition, the peak of convective activity is shifted one hour earlier. The KES analysis indicates the accumulation of energy near the tail of the spectrum between model levels 50 and 20 (Fig. 10a-d), i.e., roughly between 3 and 11 km above the ground. Lastly, the amount of small-scale features in the precipitation field increases at both $\Delta x = 0.5$ km and 1 km.

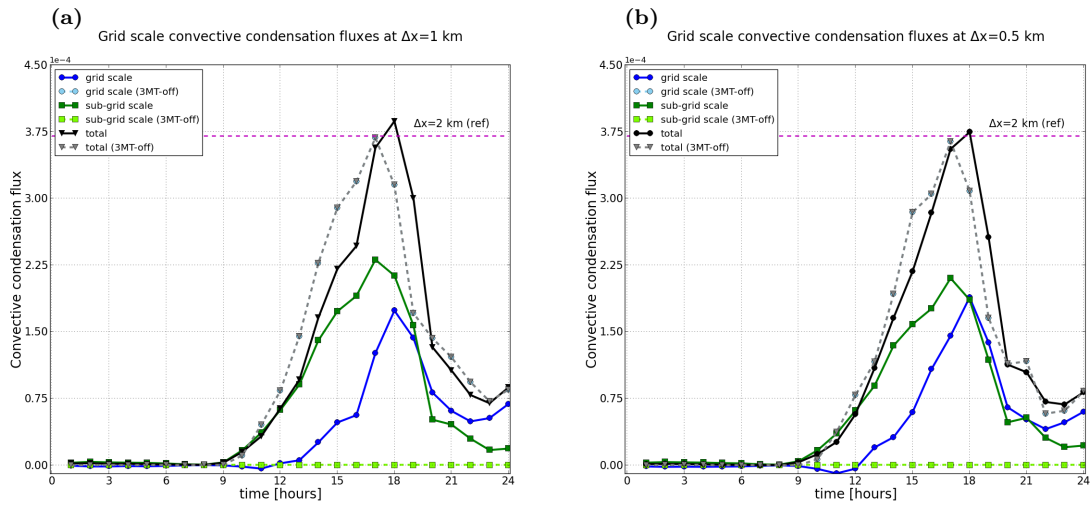


Figure 9: Spatially averaged subgrid-scale, grid-scale and total convective condensation flux for model configurations with 3MT scheme and without 3MT scheme (3MT-off) during the 21 June 2018 convection case at: (a) $\Delta x=1$ km and (b) $\Delta x=0.5$ km.

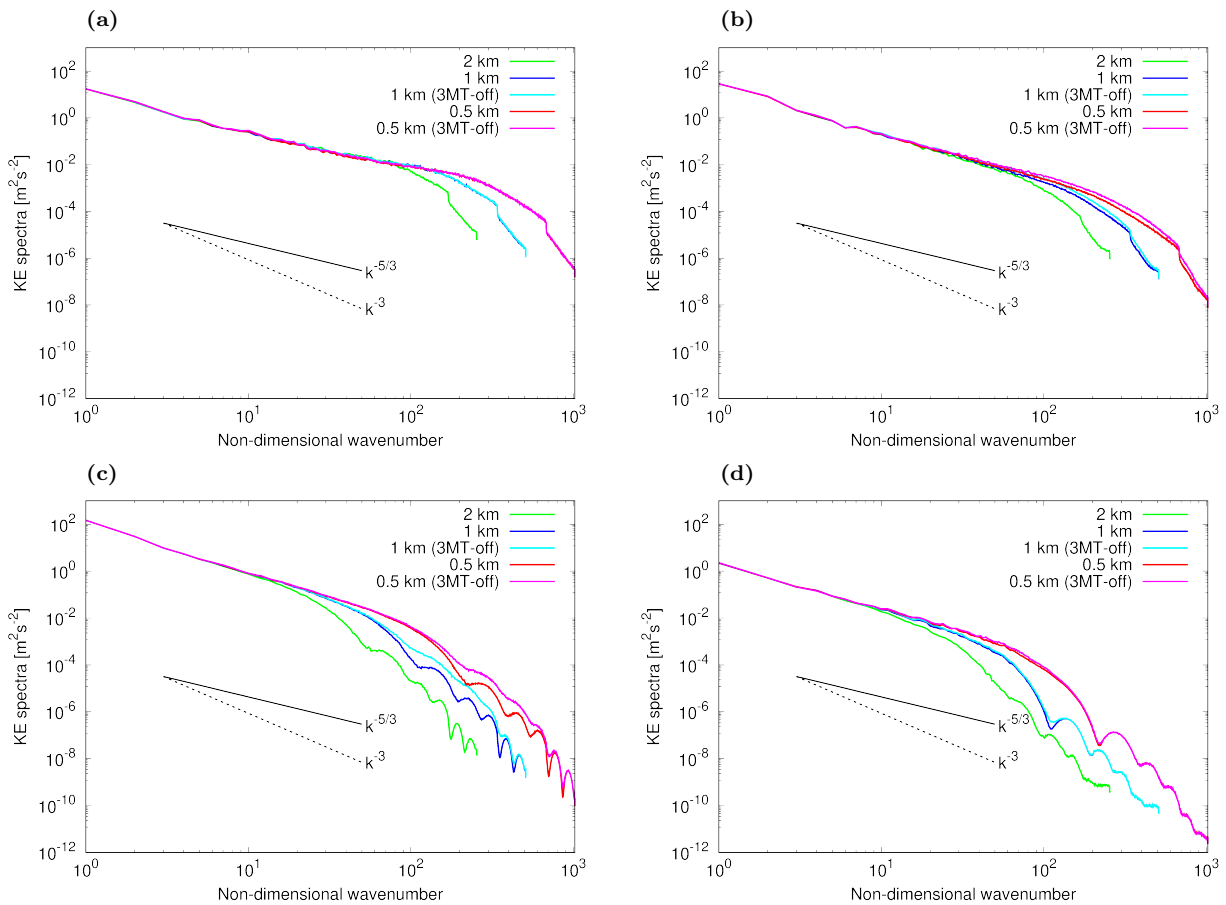


Figure 10: Kinetic energy spectra at 15 UTC 21 June 2018 for different experiments (see legend) at model levels: (a) 80, (b) 50, (c) 20 and (d) 10. The experiments containing "3MT-off" in the legend are launched without the 3MT scheme, while the remaining ones have it switched on.

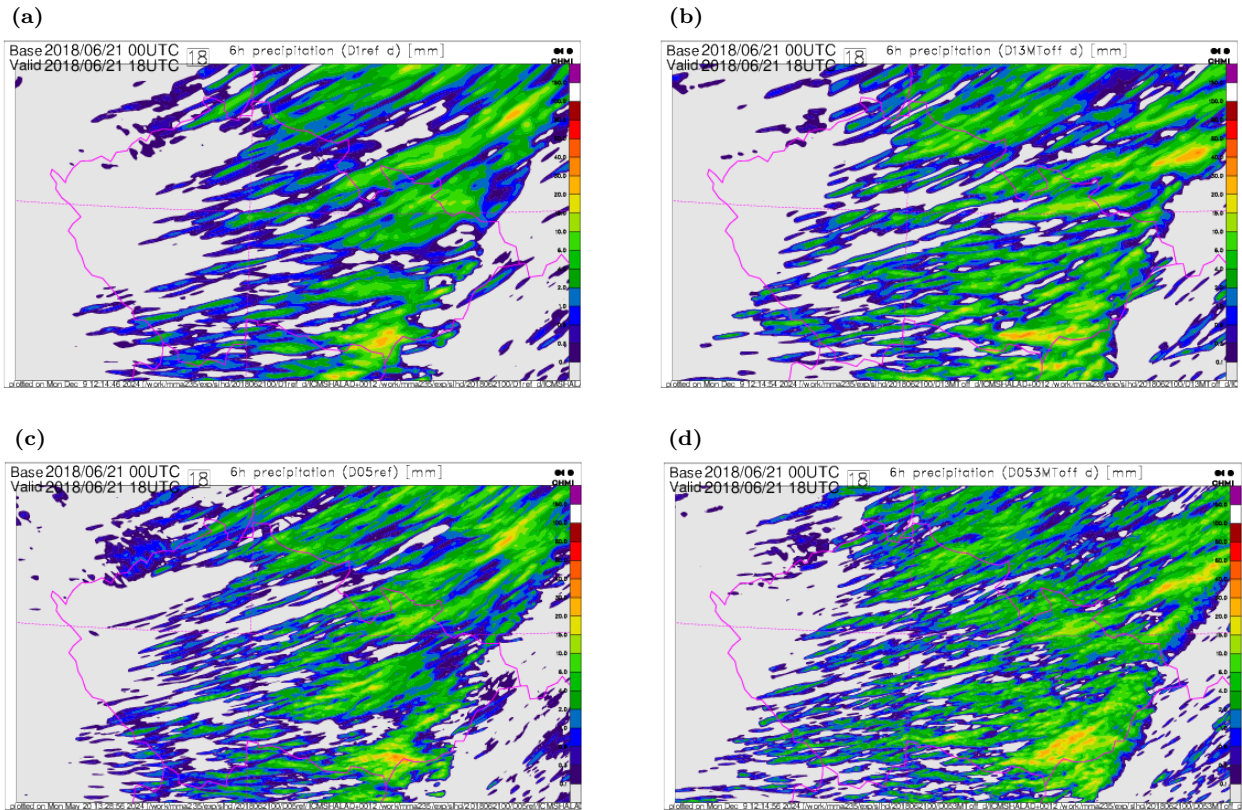


Figure 11: 6-hour accumulated total precipitation, i.e., between 12 UTC and 18 UTC on 21 June 2018 for different experiments at: (a) $\Delta x=1$ km (with 3MT), (b) $\Delta x=1$ km (without 3MT), (c) $\Delta x=0.5$ km (with 3MT) and (d) $\Delta x=0.5$ km (without 3MT).

In the 10 June 2023 case, switching the 3MT scheme off results in a reduction of total condensation flux by $\sim 20\%$, without shifting the timing of the convective peak (Fig. 12a-b). The KES analysis leads to the same conclusion as in the previous case (not shown). Finally, the precipitation patterns not only display more small-scale features (Fig. 13a-c) but also appear locally distorted and unphysical; see cauliflower-like structures in Fig. 13c.

Conclusively, given the different adaptation of the 3MT scheme to the change in Δx in the two convective cases and deteriorated results when it is switched off, further attempts will focus on its tuning. In addition, its interaction with the pseudo-3D turbulence scheme will be examined by testing the improved 3MT scheme in combination with progressively stronger pseudo-3D configurations.

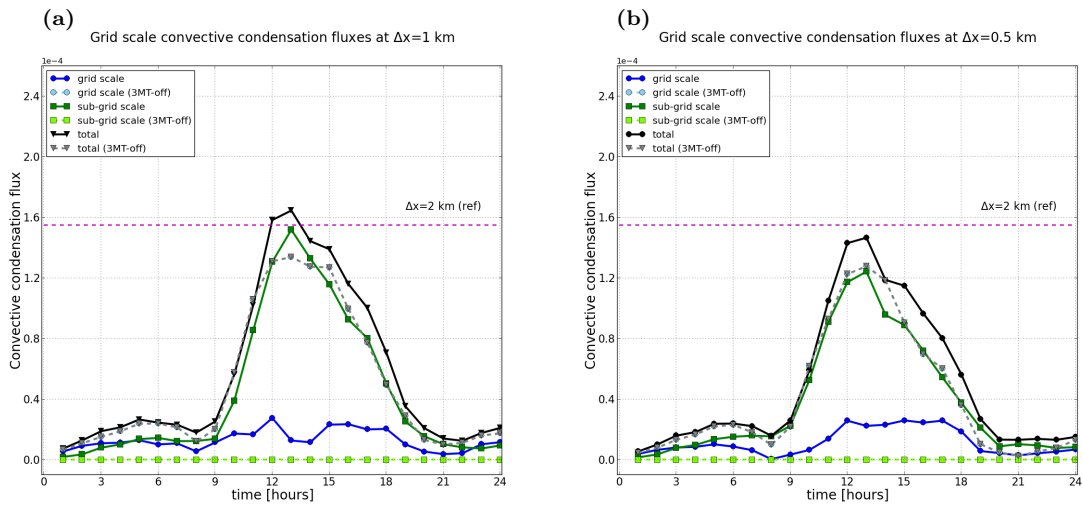


Figure 12: Spatially averaged subgrid-scale, grid-scale and total convective condensation flux for model configurations with 3MT scheme and without 3MT scheme (3MT-off) during the 10 June 2023 convection case at: (a) $\Delta x = 1$ km and (b) $\Delta x = 0.5$ km.

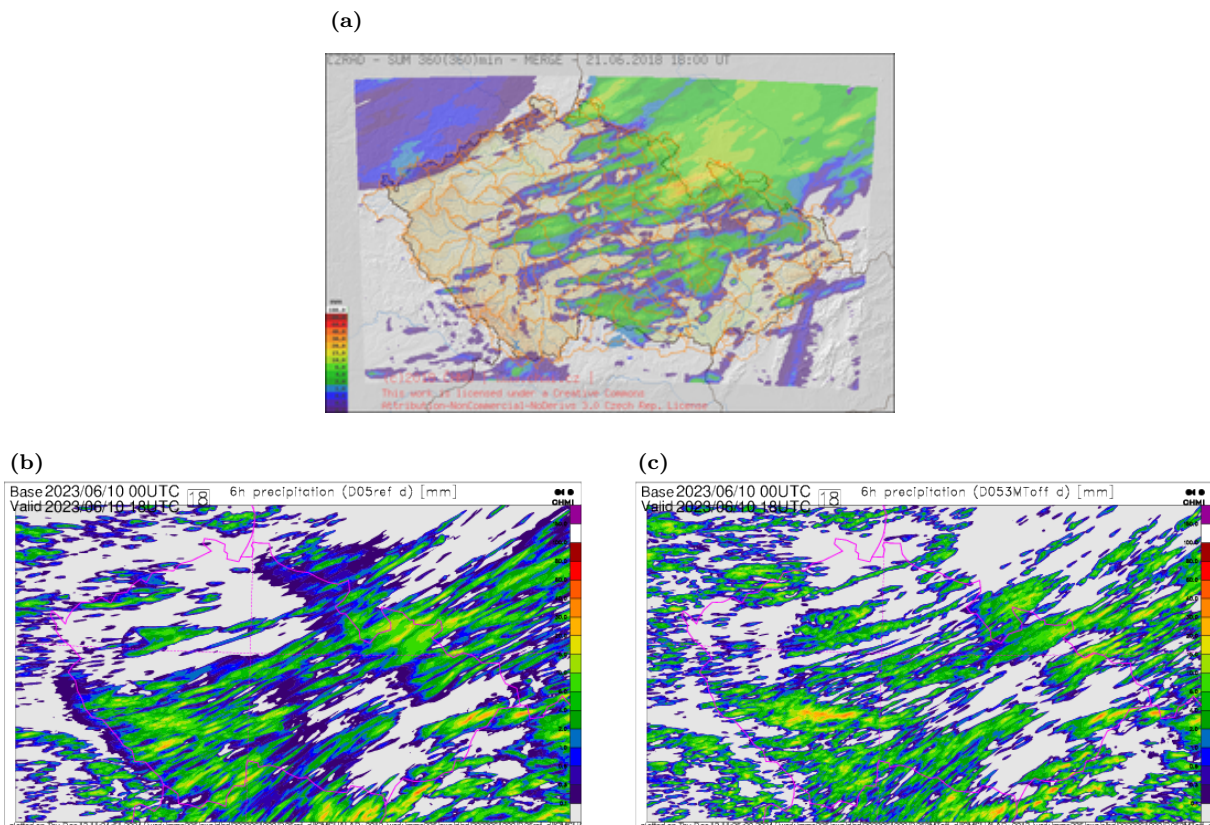


Figure 13: 6-hour accumulated total precipitation, i.e., between 12 UTC and 18 UTC on 10 June 2023 for: (a) observations and experiments at $\Delta x = 0.5$ [km] (b) with 3MT scheme and (c) without 3MT scheme.

5 Conclusion and further work

During this stay, the impact of pseudo-3D turbulence and 3MT schemes on two convection events was investigated. In doing so, tuning the intensity of the 1D + 2D component via C'_K and protecting $L_H^{K'}$, affecting also the computation of prognostic energies by adding the horizontal shear effect, proved essential. Thereby, both these effects resulted in (i) necessary decrease in TKE_{res} and TKE_{tot} at $\Delta x=0.5\text{km}$, (ii) removal of kinetic energy near the tail of the spectrum and (iii) reducing noise in prognostic fields, e.g., pressure departure and precipitation. Furthermore, the associated precipitation patterns align more closely with observed data. However, although the settings of the quasi-3D scheme seem reasonable for the convective case with large-scale forcing (21 June 2018), they produce too strong diffusion for a more localized convection case (10 June 2023). Therefore, further adjustments are needed.

The role of the 3MT scheme proved important in the two analyzed cases and remains necessary at both $\Delta x=0.5\text{ km}$ and 1 km . Further tuning activities are foreseen, primarily focusing on additional adjustments to the RMULACVG parameter. The impact and adaptation capabilities of the shallow convection scheme, being an integral component of the TOUCANS turbulence parameterization, should also be investigated.

Finally, the parameterization of the horizontal shear effects to the pair of turbulence prognostic energies may be revised. Thereby, for consistency reasons, horizontal momentum fluxes can be adopted from the 1D + 2D scheme, while the horizontal TKE components can be extracted by employing Eqs. (15a)-(15b) of [12].

Acknowledgment: The author wishes to thank to Petra Smoliková and Radmila Brožková for their support and cooperation, as well as to entire ONPP department for their warm welcome and hospitality. This stay is funded by the RC-LACE project.

References

- ¹I. Bařtak Duran, J.-F. Geleyn, and F. Vana. A Compact Model for the Stability Dependency of TKE Production–Destruction–Conversion Terms Valid for the Whole Range of Richardson Numbers. *J. Atmos. Sci.*, 71:3004–3026, 2014.
- ²I. Bařtak Duran, J. F. Geleyn, F. Vana, J. Schmidli, and R. Brořkova. A Turbulence Scheme with Two Prognostic Turbulence Energies. *J. Atmos. Sci.*, 75:3381–3402, 2018.
- ³P. Termonia, C. Fischer, E. Bazile, F. Bouyssel, R. Brořkova, P. Benard, B. Bochenek, D. Degrauwe, M. Derkova, R. El Khatib, R. Hamdi, J. Mařek, P. Pottier, N. Pristov, Y. Seity, P. Smolikova, O. řpaniel, M. Tudor, Y. Wang, C. Wittmann, and A. Joly. The ALADIN System and its canonical model configurations AROME CY41T1 and ALARO CY40T1. *Geosci. Model Dev.*, 11:257–281, 2018.
- ⁴B. Goger, M. W. Rotach, A. Gohm, O. Fuhrer, I. Stiperski, and A. A. M. Holtslag. The impact of three-dimensional effects on the simulation of turbulence kinetic energy in a major alpine valley. *Bound.-Layer Meteor.*, (168):1–27, 2018.
- ⁵Rotach M.W. Gohm A. Stiperski I. Fuhrer O. Goger, B. and G. de Morsier. *J. Appl. Meteorol. Climatol.*, page 2087–2102.
- ⁶Bařtak Duran, I. *TOUCANS documentation (15th July version)*. RC-LACE, 2015.
- ⁷W. Wang, B. Liu, L. Zhu, Z. Zhang, A. Mehra, and V. Tallapragada. A new horizontal mixing-length formulation for numerical simulations of tropical cyclones. *Wea. Forecasting*, 36:679–695, 2021.
- ⁸M. Hrastinski. Implementation of the quasi-3D turbulence scheme within the ALARO Canonical Model Configuration. RC-LACE stay report, CHMI, Prague, Czech Republic, 25 April - 20 May, 2022.
- ⁹J. Smagorinski. General circulation experiments within the primitive equations. *Mon. Wea. Rev.*, (91):99–164, 1963.
- ¹⁰M. Hrastinski. Towards the pseudo 3D turbulence within the ALARO CMC. RC-LACE stay report, CHMI, Prague, Czech Republic, 13-24 May, 2024.
- ¹¹M. Hrastinski. Development of the sub-kilometer ALARO Canonical Model Configuration. RC-LACE stay report, CHMI, Prague, Czech Republic, 15-26 May and 9-20 October, 2023.
- ¹²Y. Cheng, V. M. Canuto, and A. M. Howard. An Improved Model for the Turbulent PBL. *J. Atmos. Sci.*, 59:1550–1565, 2002.